Orange G degradation by heterogeneous peroxymonosulfate activation based on magnetic MnFe$_2$O$_4$/α-MnO$_2$ hybrid

Abstract

Wastewater containing an azo dye Orange G (OG) causes massive environmental pollution, thus it is critical to developing a highly effective, environmental-friendly, and reusable catalyst in peroxymonosulfate (PMS) activation for OG degradation. In this work, we successfully applied a magnetic MnFe$_2$O$_4$/α-MnO$_2$ hybrid fabricated by a simple hydrothermal method for OG removal in water. The characteristics of the hybrid were investigated by XRD, SEM, EDX, FT-IR, BET, VSM, and XPS. The effects of operational parameters (i.e., catalytic system, catalytic dose, solution pH, and temperature) were investigated. The results exhibited that 96.8% of OG degradation was obtained with MnFe$_2$O$_4$/α-MnO$_2$(1:9)/PMS system in 30 min regardless of solution pH changes. The radical quenching experiments demonstrated that $SO_4^{\bullet-}$, $O_2^{\bullet-}$, and $^1O_2$ were the primary reactive oxygen species responsible for the OG degradation. The hybrid also displayed unusual stability with less than 30% loss in the OG removal after four sequential cycles. Overall, magnetic MnFe$_2$O$_4$/α-MnO$_2$ hybrid could be used as a high potential activator of PMS to remove orange G and maybe other dyes from wastewater.

Keywords: MnFe$_2$O$_4$/α-MnO$_2$, peroxymonosulfate, Orange G, catalytic degradation, reusability

1. Introduction

Processing industries such as dyeing, printing, textiles, and leather generate a massive amount of polluted wastewater that contains hazardous organic compounds (e.g., orange G, orange II phenol, methyl violet, and methylene blue) (Ejder-Korucu *et al.*, 2015). Orange G (OG) (**Figure 1**), which is an acidic and widely used azo compound in the dyeing of fabrics, has been gained

25   much attention due to its non-biodegradable, toxic, and potentially carcinogenic nature (Cai *et al.*,

26   2011). Therefore, the physicochemical treatment of OG-containing wastewater is necessary to

27   reduce its environmental pollution. Treatments of wastewater involved oxidation methods (e.g.,

28   photocatalytic oxidation, ozone/hydrogen peroxide-induced oxidation, and Fenton reaction-based

29   oxidation), physical methods (e.g. adsorption and filtration), and biological methods (e.g., aerobic

30   and anaerobic decomposition with fungi, bacteria, and algae) (Javaid and Qazi, 2019; Wang and

31   Zhuan, 2020; Garrido-Cardenas *et al.*, 2019). Recently, advanced oxidation processes (AOPs)

32   have received great interest from researchers since they brought good efficiency in wastewater

33   treatment (M'Arimi *et al.*, 2020). Among the AOPs, sulfate radical-advanced oxidation processes

34   (SR-AOPs) have been widely studied because of their superiorities of (i) greater standard

35   oxidation-reduction potential of sulfate radical ($SO_4^{\bullet-}$) (E_o = 2.5-3.1 V *vs.* normal hydrogen

36   electrode (NHE)) than that of hydroxyl radical ($HO^{\bullet}$) (E_o = 1.8-2.7 V *vs.* NHE), (ii) broader range

37   of reaction pH conditions of $SO_4^{\bullet-}$ (pH 2-8) than that of $OH^{\bullet}$ (pH 2-4, an acidic environment), (iii)

38   longer half-life of $SO_4^{\bullet-}$ ($t_{1/2}$ = 30-40 µs) compared with that of $OH^{\bullet}$ ($t_{1/2} \leq 1$ µs), and (iv) higher

39   oxidation capacity in both carbonate and phosphate buffer solutions (Xia *et al.*, 2020). Sulfate

40   radicals can be effectively produced through the activation of persulfate (PS, $S_2O_8^{2-}$) and

41   peroxymonosulfate (PMS, HSO_5^-), which contain labile peroxide bonds (O-O). In comparison with

42   PS, PMS has been more immensely utilized for its asymmetrical molecular structure, lower

43   peroxide bond dissociation energy, and lesser redox potential (1.77 V *vs.* 2.01 V) (Ma *et al.*, 2021).

44   In general, PMS can be activated to generate sulfate radicals through the presence of physical (e.g.,

45   heating, ultraviolet (UV) irradiation, and ultrasonic waves) and chemical activation methods (e.g.,

46   transition metal ion-based catalysts (iron (Fe^{2+}), cobalt (Co^{2+})), alkaline, and strong oxidizers)

47   (Peng *et al.*, 2021). Among these agents, the transition metal ion-based catalysts gained the most

48 interest for their low energy consumption and simplicity of the PMS activation (Li *et al.*, 2021).

49 In particular, heterogeneous systems of these metal ion catalysts were intensively investigated

50 because of their stable structure, high interactive surface area, and easy recovery (Fan *et al.*, 2017).

51 Nevertheless, the major concerns in the utilization of compounds such as Co^{2+} and Fe^{2+} ions were

52 the secondary pollution and potential biological toxicity due to the unexpected release of Co^{2+} and

53 a remarkable reduction in the generation efficiency of sulfate radicals if used in high iron loading

54 quantities, respectively (Hu and Long, 2016). The above-mentioned limitations can partially be

55 surmounted with heterogeneous systems of manganese oxides/ions because of their stability, high

56 catalytic activity, environmental-friendliness, and low cost (Huang and Zhang, 2019). Manganese

57 dioxide (MnO_2) has many different morphologies such as α-, β-, and γ-MnO_2, and each phenotype

58 exhibits unique features (Dong *et al.*, 2014). In this regard, α-MnO_2 presented the highest catalytic

59 activity that can be ascribed to its high surface area and preferable crystalline structure (Xie *et al.*,

60 2015). However, α-MnO_2 is a heterogeneous catalyst, which interferes with the subsequent catalyst

61 separation and recovery, thereby disturbing its applicability (Uematsu *et al.*, 2016). On the contrary,

62 spinel ferrite $MnFe_2O_4$ has stable, insoluble, and excellent magnetic properties, which make it easy

63 to be separated from the reaction solution (Shao *et al.*, 2012; Yao *et al.*, 2014). These observations

64 suggested the fabrication of a heterogeneous catalyst system via a combination between α-MnO_2

65 and $MnFe_2O_4$.

66 In fact, Chen *et al.* (2019) successfully synthesized magnetic $MnO_2/MnFe_2O_4$

67 nanocomposite by hydrothermal method and applied it to activate PMS for Rhodamine B (RhB)

68 degradation. The study's results displayed that the RhB decomposition efficiency of the

69 $MnO_2/MnFe_2O_4$ nanocomposite (with a molar ratio of 7:1) was 90% within 5 min in the presence

70 of PMS. However, the formation mechanism of the $MnO_2/MnFe_2O_4$ nanocomposite was not

71   discussed with the lack of TGA and EDX-mapping analyses and the material had a low surface

72   area of 67.2 m^2/g. Besides, the material was strongly affected under alkaline environments but the

73   effect of pH was not thoroughly discussed. For other organic pollutants, $MnFe_2O_4$/δ-MnO_2 (Zhu

74   *et al.*, 2021) and α-MnO_2/$MnFe_2O_4$ (Xu *et al.*, 2021) were fabricated for PMS activation in

75   degradation sulfadiazine and norfloxacin, respectively, in water. However, the results of TGA and

76   EDX-mapping as well as the formation mechanism of $MnFe_2O_4$ were not provided. Also, the role

77   of superoxide radical ($O_2^{\bullet-}$), and especially, singlet oxygen ($^1O_2$) in the reaction mechanism has

78   not been deeply studied. Therefore, a systematic study, which focuses on the formation mechanism

79   of the material and the reaction mechanism in PMS activation for dye, especially popular OG, is

80   needed not only for understanding the formation and activity of the material but also for

81   determining the suitable reaction conditions for further practical application in dye removal by

82   PMS activation.

83   In this work, we prepared a magnetic $MnFe_2O_4$/α-MnO_2 hybrid via the hydrothermal method

84   and investigated the decomposition efficiency of orange G through the hybrid-catalyzed PMS

85   activation. The physical and chemical properties of the hybrid material were examined by various

86   characterization techniques. The effects of environmental factors such as catalyst dosage, PMS

87   dosage, OG concentration, pH, temperature, and catalyst reusability on the PMS activation were

88   investigated. In addition, the possible degradation mechanisms of the $MnFe_2O_4$/α-MnO_2/PMS

89   system for OG degradation were also determined.

90   **2. Materials and Methods**

91   **2.1. Materials**

92   Manganese (II) chloride tetrahydrate ($MnCl_2.4H_2O$), ferric chloride hexahydrate

93   ($FeCl_3.6H_2O$), potassium peroxymonosulfate or PMS ($KHSO_5 \cdot 0.5KHSO_4 \cdot 0.5K_2SO_4$, trade name

94 Oxone®), sodium persulfate ($Na_2S_2O_8$), potassium permanganate ($KMnO_4$), anhydrous sodium

95 acetate (CH_3COONa), ethylene glycol (EG, $(CH_2OH)_2$), polyethylene glycol (PEG), ethanol

96 (CH_3CH_2OH, 99.5%), *tert*-butyl alcohol (TBA, $(CH_3)_3COH$), orange G (OG) were all obtained

97 from Shanghai Aladdin Bio-Chem Technology Co., Ltd. (Shanghai, China). All reagents used in

98 this work were of analytical grade and used without further purification unless otherwise stated.

99 **2.2. Synthesis of MnFe$_2$O$_4$/α-MnO$_2$ hybrid**

100 **2.2.1. Synthesis of α-MnO$_2$ nanoparticles**

101 The α-MnO_2 nanoparticles were prepared by a hydrothermal method (Ma *et al.*, 2011). In

102 brief, 0.363 g of $KMnO_4$ was completely dissolved in 80 mL of deionized water. Then 0.8 mL of

103 concentrated HCl solution (37%) was slowly added to the above aqueous $KMnO_4$ solution and

104 stirred for 1 h. Next, the mixture was transferred into a 100-mL Teflon-lined stainless steel

105 autoclave and treated at 150 ^{o}C for 12 h. After the reaction, the mixture was cooled down to an

106 ambient temperature. The obtained dark product was consecutively washed three times with

107 deionized water and ethanol before drying in a vacuum oven at 80 °C for 3 h.

108 **2.2.2. Synthesis of magnetic MnFe$_2$O$_4$ nanoparticles**

109 The MnFe$_2$O$_4$ nanoparticles were also synthesized by a solvothermal method with slight

110 modification (Reddy and Mohamed, 2015). Briefly, 1.092 g of $FeCl_3.6H_2O$ and 0.254g of

111 $MnCl_2.4H_2O$ were dissolved in 100 mL of EG, and the mixture was stirred for 30 min. After that,

112 7.242 g of CH_3COONa and 2.0 g of polyethylene glycol (PEG) were sequentially added to the

113 above mixture and stirred for 1 h. The resulting mixture was then transferred into a 100-mL

114 Teflon-lined stainless-steel autoclave and treated at 200 ^{o}C for 12 h. After the reaction, the mixture

115 was cooled down to an ambient temperature. The black product was separated by a magnet and

116   consecutively washed three times with deionized water and ethanol, and finally dried in a vacuum

117   oven at 80 °C for 6 h.

118   **2.2.3. Synthesis of magnetic MnFe$_2$O$_4$/α-MnO$_2$ hybrid**

119   The MnFe$_2$O$_4$/α-MnO$_2$ hybrid was also fabricated using a hydrothermal method (Chen *et al.*,

120   2019) (**Figure 2**). In detail, 0.5 g of as-prepared MnFe$_2$O$_4$ was added into 100 mL of deionized

121   water, and the dispersion was sonicated in a water bath for 30 min. Later, 0.856 g of KMnO$_4$ and

122   1.812 mL of concentrated HCl solution (37%) were serially added into the above dispersion, and

123   the mixed solution was mechanically stirred for 1 h. The mixture was then transferred into a 100-

124   mL Teflon-lined stainless steel autoclave and treated at 150 °C for 12h. After the reaction, the

125   mixture was cooled down to an ambient temperature. The resultant product was continuously

126   washed three times with deionized water and ethanol and dried in a vacuum oven at 80 °C for 3 h.

127   To investigate the effective catalytic activity, the hybrids with various mass ratios of MnFe$_2$O$_4$:α-

128   MnO$_2$ (i.e., 1:5, 1:7, and 1:9) were prepared.

129   **2.3. Characterization of materials**

130   To confirm the crystalline structure, X-ray diffraction (XRD) patterns of the as-synthesized

131   α-MnO$_2$, MnFe$_2$O$_4$, and MnFe$_2$O$_4$/α-MnO$_2$ hybrid were recorded on a Bruker D8 Advance X-ray

132   diffractometer with Cu-Kα radiation (λ = 1.5418°A), operating at 30 kV and 40 mA. In addition,

133   the size, morphology, and microstructure of these materials were determined using field emission

134   scanning electron microscopy (FE-SEM, Hitachi SU810, Japan) incorporated with an energy-

135   dispersive X-ray (EDX) analyzer (EMAX Energy, Horiba Ltd., Japan). The chemical composition

136   and elemental valence states of the materials were identified by X-ray photoelectron spectroscopy

137   (XPS, Kratos AXIS Ultra DLD). Thermogravimetric analysis (TGA) was carried out by using

138   Pyris 6 TGA Perkin Elmer. The chemical bonds of the materials were confirmed by Fourier

139   transform infrared spectroscopy (FT-IR, Perkin Elmer BX) with the scanned wavenumber in the

140   range of 4000–400 cm^{-1}. The specific surface area of the materials was examined by a Brunauer–

141   Emmett–Teller method (BET, Micromeritics ASAP 2460) with the degassing process at 300 °C

142   for 4 h before each measurement. The magnetic properties of the synthesized materials were

143   identified by a vibrating sample magnetometer equipped with a 1 T magnet (PMC MicroMag 3900

144   model).

145   The isoelectric point of the hybrid material was determined by the titration method. Six 50-

146   mL flasks were added with 25 mL of 0.1 M NaCl solution and initial pH values of the solution

147   (pH_i) were adjusted to range from 3 to 11 using 0.1 M HCl or NaOH solutions. Each flask was

148   then added with 0.05 g of the hybrid material and shaken by a shaker for 48 h. The suspension was

149   then settled and filtered, and the filtrate was sent for final pH measurement (pH_f). A graph was

150   then plotted for the relationship of difference between pH values ($\Delta pH = pH_f - pH_i$) according to

151   pH_i and the pH value at which $\Delta pH = 0$ is determined as the isoelectric pH value (pH_{pzc}) of the

152   material.

153   **2.4. Catalytic activity experiments**

154   At first, stock suspensions of $MnFe_2O_4/\alpha-MnO_2$, orange G (OG), potassium

155   peroxymonosulfate (PMS) with concentrations of 1000, 100, 5000 mg/L, respectively, were

156   prepared by dispersing the pre-weighed amounts of respective chemicals in deionized water using

157   volumetric flasks.

158   In the typical experiment to determine the catalytic activity of $MnFe_2O_4/\alpha-MnO_2$ in PMS

159   activation, the OG degradation test was performed at room temperature (30±2 °C). In a 5-mL

160   volumetric flask, 0.5 mL of $MnFe_2O_4/\alpha-MnO_2$ stock suspension was added into 2.5 mL of OG

161   stock solution and followed by solution pH adjustment using 0.05 M H_2SO_4 or 0.05 M NaOH

162 solutions. The suspension was then shaken for 30 min until approaching the adsorption-desorption

163 equilibrium. Subsequently, 1.00 mL of PMS stock solution was added to the above mixture under

164 shaking to initiate an oxidation reaction. At pre-determined time points, the mixed solution in the

165 flask was transferred into a quartz cuvette, and the UV/Vis absorbance of the OG solution was

166 measured at 480 nm. The control solutions were also prepared in the same procedure with the

167 absence of OG.

168   In the specific experiment to investigate the effect of temperature on OG degradation, 10.0

169 mL of $MnFe_2O_4/\alpha$-MnO_2 suspension was added into 50.0 mL of OG stock solution and followed

170 by the adjustment of initial pH. The mixture was then shaken for 30 min to reach the adsorption-

171 desorption equilibrium. Afterward, 20.0 mL of PMS stock solution was added to the above mixture

172 under shaking. The assigned temperature values (i.e., 20, 30, and 40 °C) were set. At pre-

173 determined time intervals, 0.2 mL of Na_2SO_3 (1.0 M, as a reaction terminator) was added into a

174 4.0 mL aliquot of the sample, and then the UV/Vis absorbance of OG was measured at 480 nm.

175 After the reaction, the hybrid was separated by a magnet, washed three times with deionized water

176 and ethanol, and then dried in a vacuum oven at 80 °C for 12 h. The stability and reusability of the

177 $MnFe_2O_4/\alpha$-MnO_2 hybrid were assessed by re-using the recycled catalyst after three consecutive

178 reaction cycles. The quenching tests of reactive radicals were performed by adding a certain

179 amount of TBA, EtOH, and FFA (at 100 mM) and p-BQ (at 10 mM) into the reaction mixtures.

180   The decomposition efficiency of OG was calculated using the following equation:

181 $$H\% = \left(1 - \frac{C_t}{C_0}\right).\,100\,(\%) = \left(1 - \frac{A_t}{A_0}\right).\,100\,(\%) \qquad \text{(Eq. 1)}$$

182 Where C_o and A_o are the concentration and absorbance, respectively, of OG at the initial

183 time. C_t and A_t are the concentration and absorbance, respectively, of OG at a defined time t.

184   The kinetics of the OG decomposition by the $MnFe_2O_4/\alpha$-MnO_2/PMS system was expressed

185   through a pseudo-first-order model as follows:

186                                    $LnC_t/C_o = -k_{app}.t$ (Eq. 2)

187   Where C_o and C_t are the OG concentrations at the initial time and determined time t,

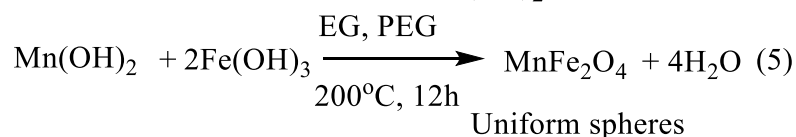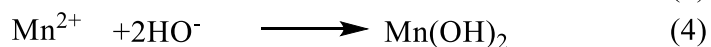188   respectively and k_{app} is the apparent rate constant (min^{-1}).

189   **3. Results and discussion**

190   **3.1. Material characterizations**

191   The morphologies of α-MnO_2, $MnFe_2O_4$, and $MnFe_2O_4/\alpha$-MnO_2 were characterized by SEM.

192   As shown in **Figures 3a and 3b**, the α-MnO_2 was observed in smooth-surfaced and uniformly

193   distributed rod-like structures, with dimensions of 0.5-1 μm in length and 50-100 nm in diameter.

194   (Ma *et al.*, 2011; Huang *et al.*, 2020). The rod structure formation of α-MnO_2 can be explained

195   through its multi-stage synthetic procedure of nucleation - dissolving - anisotropic growth -

196   recrystallization (Zhang *et al.*, 2014). In the early stages, the MnO_2 crystalline seeds were

197   generated by a redox reaction between Cl$^-$ and MnO_4^- in an acidic medium, then developing into

198   MnO_2 with a 1-D rod structure at a low temperature of 120 ^{o}C and low pressure (Reaction 1).

199   Subsequently, the second stage, which was performed at higher temperature and pressure and

200   prolonged hydrothermal time, made the MnO_2 rods grow longer and larger, and the rods were

201   gradually converted into rod-cluster morphology (Ma *et al.*, 2011; Huang *et al.*, 2020). Zhu *et al.*

202   (2021) showed that a 3-D hierarchical corolla-like structure of δ-MnO_2 was formed at a low

203   synthetic temperature of 100 ^{o}C. Thus, the temperature played an important role in the formation

204   of structural and morphological forms of MnO_2.

$$2KMnO_4 + 8HCl \xrightarrow[12h]{150^oC} \alpha\text{-}2MnO_2 + 3Cl_2 + 2\,KCl + 4H_2O \qquad (1)$$

205

206
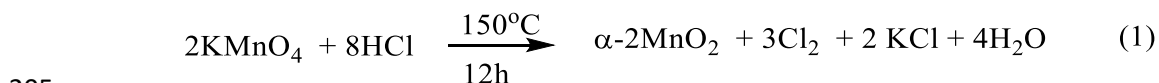
207   In addition, $MnFe_2O_4$ were presented as uniform spheres, which possess diameters in the

208   range of 0.1-0.15 μm (**Figures 3c and 3d**). The mechanism for the formation of spherical $MnFe_2O_4$

209   nanoparticles could be explained in the following steps. First of all, sodium acetate (CH_3COONa)

210   was hydrolyzed to elicit an alkaline medium (Reaction 2). The Fe^{3+} and Mn^{2+} ions then react with

211   the hydroxyl anion (HO^-) to form precipitates of iron (III) and manganese (II) hydroxides,

212   respectively (Reactions 3 and 4). Finally, $Fe(OH)_3$ and $Mn(OH)_2$ were converted to $MnFe_2O_4$

213   through the dewatering process shown in Reaction 5 (Reddy and Mohamed, 2015). EG not only

214   acts as a solvent but also plays an important role in controlling the size and morphology of the

215   particles in solvothermal systems. Meanwhile, PEG serves as a structure-directing agent, as it can

216   easily self-assemble to form spherical grains, thereby coating the $MnFe_2O_4$ particle surface.

217   Besides, PEG can act as a protective layer that prevents the agglomeration of the particles and

218   minimizes the direct exposure of the ferrite surface to an unexpected environment (Reddy and

219   Mohamed, 2015; Kurtan *et al.*, 2016).

$$CH_3COO^- + H_2O \longrightarrow CH_3COOH + HO^- \quad (2)$$

$$Fe^{3+} + 3HO^- \longrightarrow Fe(OH)_3 \quad (3)$$

$$Mn^{2+} + 2HO^- \longrightarrow Mn(OH)_2 \quad (4)$$

$$Mn(OH)_2 + 2Fe(OH)_3 \xrightarrow[200^oC, 12h]{EG, PEG} MnFe_2O_4 + 4H_2O \quad (5)$$

Uniform spheres

220

221   As shown in **Figures 3e** and **3f**, with the combination of $MnFe_2O_4$ and α-MnO_2, the nanorod

222   structure of MnO_2 was retained. However, since $MnFe_2O_4$ has a high tendency to be agglomerated,

223   the aggregation of $MnFe_2O_4$ can be attributed to the magnetic dipole interaction between these

224   particles. A rougher $MnFe_2O_4$/α-MnO_2 surface than α-MnO_2 can also be observed due to the

225   superposition of $MnFe_2O_4$ particles on the α-MnO_2 surface. Thus, in the hybrid materials, α-MnO_2

226   and $MnFe_2O_4$ alternate with each other, then forming pores, thereby significantly increasing the

227   surface area and the active positions to activate the PMS.

228   To determine the elemental composition in the magnetic $MnFe_2O_4/\alpha\text{-}MnO_2$ hybrid, the EDX

229   spectrum was adopted (**Figures 4a** and **4b**). According to **Figure 4a**, the Fe, Mn, and O elements

230   accounted for 30.16, 58.01, and 11.83%, respectively, in the weight percentage of the hybrid. The

231   results elicited an atomic Mn:Fe ratio of 4.993, which was consistent with the theoretically

232   calculated Mn:Fe ratio of 4.9 for the hybrid. Furthermore, EDX-mapping analysis of Mn, Fe, and

233   O elements (**Figures 4b**) confirmed the good distribution of $\alpha\text{-}MnO_2$ on the $MnFe_2O_4$ surface.

234   To determine the success in synthesis and the purity of as-prepared materials, the crystal

235   structures of $\alpha\text{-}MnO_2$, $MnFe_2O_4$, and $MnFe_2O_4/\alpha\text{-}MnO_2$ materials were investigated through XRD,

236   as shown in **Figure 5**. The synthesized $\alpha\text{-}MnO_2$ displayed typical diffraction peaks at 2θ of 12.8°,

237   18.12°, 28.84°, 37.52°, 41.96°, 50°, 60.44° and 65.28°, which could be indicated to the 100, 200,

238   310, 211, 301, 411, 521 and 002 planes, respectively (JCPDS No. 44-141) (Ma *et al.*, 2011;

239   Davoglio *et al.*, 2018). In addition, the prepared $MnFe_2O_4$ presented characteristic peaks at 29.66°,

240   34.92°, 43.04°, 56.86° and 62.76°, that sequentially attributed to the 220, 311, 400, 511 and 440

241   lattices of spinel-type $MnFe_2O_4$ nanostructures (JCPDS No. 73-1964) (Cai *et al.*, 2014; Reddy and

242   Mohamed, 2015). Importantly, the $MnFe_2O_4/\alpha\text{-}MnO_2$ clearly showed both diffraction peaks of

243   constitutive $MnFe_2O_4$ and $\alpha\text{-}MnO_2$ materials. Of note, in the XRD spectrum of $MnFe_2O_4/\alpha\text{-}MnO_2$,

244   all peak intensities were lower than that in separated constituents. Moreover, there was neither the

245   disappearance of characteristic peaks nor the presence of new peaks in the XRD pattern of the

246   hybrid, implying the integrity of $MnFe_2O_4$ and $\alpha\text{-}MnO_2$ crystal structures with high purity.

247   Consequently, these results confirmed the successful synthesis of magnetic $MnFe_2O_4/\alpha\text{-}$

248   MnO_2 hybrid by using the hydrothermal treatment.

249   **Figure 6** showed the FT-IR spectra of α-MnO_2, $MnFe_2O_4$, and magnetic $MnFe_2O_4$/α-

250   MnO_2 hybrid. The as-prepared α-MnO_2 presented characteristic peaks at 699.98 and 503.62 cm^{-1},

251   which could be attributed to Mn-O bending vibrations in MnO_6 octahedra of the α-MnO_2 nanorods

252   (Wang *et al.*, 2007). For the $MnFe_2O_4$ material, the peaks at 3243.80, 1578.10, and 1351.79 cm^{-1}

253   were ascribed to the O-H stretching vibrations (Kurtan *et al.*, 2016). Importantly, the peak at

254   539.01 cm^{-1} was specifically associated with the Mn-O stretching vibration of spinel-type

255     $MnFe_2O_4$ nanostructures (Chen *et al.*, 2019). Notably, the FT-IR spectrum of $MnFe_2O_4$/α-MnO_2

256   simultaneously displayed characteristic peaks of α-MnO_2 and $MnFe_2O_4$ at 3243.80, 1578.10, and

257   1351.79, and 699.98 cm^{-1}. These results further demonstrated the successful synthesis of the hybrid

258   and the maintenance of α-MnO_2 and $MnFe_2O_4$ crystal structures.

259   **Figure 7** displays the XPS spectra of as-synthesized $MnFe_2O_4$/α-MnO_2 hybrid. To minimize

260   the charging effects, the binding energy of the C 1s level at 284.6 eV was adopted as a reference

261   to calibrate the spectrum. As seen from **Figure 7a**, the high-intensity peaks distributed at binding

262   energy (BE) values of 529.9, 641.8-653.9, and 711.2-724.4 eV, corresponding to O 1s, Mn 2p, and

263   Fe 2p levels, respectively. In addition, the high-resolution scans of the O 1s, Mn 2p, and Fe 2p

264   peaks were presented in **Figures 7b–d**. As can be seen from Fe 2p spectrum (**Figure 7b**), the main

265   peaks at 711.2 and 724.4 eV sequentially relate to Fe $2p_{3/2}$ and Fe $2p_{1/2}$ levels, which implied the

266   occurrence of the Fe^{III} compound (Pham *et al.*, 2019). With the regard to Mn 2p spectrum, two

267   main peaks (Mn $2p_{3/2}$ and Mn $2p_{1/2}$) were observed in **Figure 7c**. The first peak including three

268   integrated peaks, which were located at BE values of 641.8, 643.5, and 653.9 eV, indicating the

269   existence of mixed-valent compounds of Mn^{II} (in $MnFe_2O_4$) and Mn^{IV} (in α-MnO_2), respectively

270   (Chen *et al.*, 2019). The O 1s spectrum in **Figure 7d** exhibits three types of the O atom in the

271   material at BE values of about 529.9, 531.4, and 532.8 eV, which were assigned to the presence

272   of lattice oxygen metal oxides (M-O or M-O-M) and dominates in the O 1s-line, hydrated metal

273   oxides (M-OH or M-O-H), and oxygen of the adsorbed water (H-O-H), respectively (Zhu *et al.*,

274   2021). These results indicated that the $MnFe_2O_4/\alpha-MnO_2$ hybrid was well-prepared.

275   To investigate the thermal stability and decomposition of the materials, the

276   thermogravimetric analysis (TGA) was performed (**Figure 8**). As shown in **Figure 8a**, the

277   thermogram curve of $\alpha-MnO_2$ exhibits three different stages of weight loss. The first stage

278   appeared when the temperature heated up from 100 to 600 °C with a weight loss of about 2.50%,

279   which can be ascribed to the evaporation of adsorbed water on the surface of the material. The

280   second stage happened in the temperature range between 600 and 700 °C with a weight loss of

281   4.50%, which can be associated with the structural transformation from $\alpha-MnO_2$ to Mn_2O_3-bixbite.

282   When the temperature increases to 870 °C, an additional weight loss of 0.88% was observed, which

283   can be caused by the transformation from Mn_2O_3-bixbite to Mn_3O_4. The MnO_2 material has

284   different crystalline structures of $\alpha-MnO_2$, $\beta-MnO_2$, and $\gamma-MnO_2$, and the TGA thermal analysis

285   scheme can be used to differentiate these types of existence. In this regard, the $\beta-MnO_2$ shows

286   thermal stability with only one weight loss (transformation of MnO_2 to Mn_2O_3), the $\gamma-MnO_2$

287   exhibits two weight reductions (surface water loss and transformation of MnO_2 to Mn_2O_3,

288   respectively), and the $\alpha-MnO_2$ displays three stages in the weight loss process (loss of surface

289   adsorbed water, transformations of MnO_2 to Mn_2O_3, and Mn_2O_3 to Mn_3O_4, respectively) (Pham *et*

290   *al.*, 2019). With the regard to $MnFe_2O_4$, the thermogram curve presents two main stages of weight

291   loss (**Figure 8b**). The first stage took place at a temperature of 200 °C with a weight loss of around

292   8.00%, which can be attributed to the water loss. At over 200 °C, an additional 2.00% of weight

293   loss was adopted. **Figure 8c** displays the weight decomposition processes of the $MnFe_2O_4/\alpha-$

294   MnO_2 hybrid. At first, when the temperature increased up to 220 °C, the weight loss of the material

295 was about 6.25%, which mainly due to the water evaporation. Subsequently, when the temperature

296 in a range of 220-650 $^{\circ}$C, a further 5.75% of weight loss was obtained, which can be related to the

297 structural transformation from α-MnO$_2$ to Mn$_2$O$_3$-bixbite. At above 650 $^{\circ}$C, an additional weight

298 loss of about 1.01% can be associated with the evolution from Mn$_2$O$_3$-bixbite to Mn$_3$O$_4$.

299   Surface area and pore parameters of the catalysts have a tremendous effect on the adsorption

300 and catalytic capability because high surface area evokes more adsorption and active sites on the

301 catalyst to meet oxidant for the pollutant degradation. The N$_2$ adsorption/desorption isotherm and

302 the pore size distribution of MnFe$_2$O$_4$/α-MnO$_2$ are presented in **Figures 9a** and **9b**, respectively.

303 Relied on the IUPAC categorization, the MnFe$_2$O$_4$/α-MnO$_2$ hybrid displays a type IV isotherm

304 with a type H3 hysteresis loop at a relative pressure (P/P$_0$) in the range of 0.4-0.98, which implies

305 a mesoporous structure of the hybrid (**Figure 9a**) (Chen *et al.*, 2019). In addition, as shown in

306 **Figure 9** and **Table 1**, MnFe$_2$O$_4$/α-MnO$_2$ exhibits a narrow pore diameter distribution in a range

307 of 2-50 nm, which was in accordance with the changes of the surface area (Sotomayor *et al.*, 2018).

308 Furthermore, as seen in **Table 1**, the specific surface area of the hybrid was 102.12 m^2/g, which

309 was greater than that in MnFe$_2$O$_4$ (98.58 m^2/g) and other catalysts in previous studies of around

310 67.0 m^2/g (Chen *et al.*, 2019). Moreover, the pore volume of the hybrid was 0.199 cm^3/g, which

311 was much higher than that of α-MnO$_2$ (0.036 cm^3/g) and MnFe$_2$O$_4$ (0.047 cm^3/g) (**Table 1**). The

312 increase in surface area and pore volume could be attributed to the co-existence and

313 interminglement of MnFe$_2$O$_4$ and α-MnO$_2$ with different morphologies in the hybrid MnFe$_2$O$_4$/α-

314 MnO$_2$. The large specific surface area implies a high number of adsorption and reactive sites on

315 the hybrid, thereby possibly resulting in an enhancement in catalytic capability.

316   As displayed in **Figure 10**, the magnetic properties of the MnFe$_2$O$_4$/α-MnO$_2$ hybrid were

317 examined by the VSM method at room temperature. The results showed that the hybrid presented

318   a typical S-shaped magnetization curve when applying a magnetic field. In addition, the hybrid

319   displays a low saturation magnetization value of 9.03 emu/g, which results in an easy separation

320   and reusability of the hybrid from the wastewater by applying an external magnetic field and

321   eventually a reduction in the consumption of catalyst as well as the secondary pollution.

3.2. Performance evaluation of the hybrid

3.2.1. Evaluation of catalytic activity and effect of different mass ratio of $MnFe_2O_4/\alpha\text{-}MnO_2$

324   At first, different systems were investigated for determining the catalytic effect of the

325    $MnFe_2O_4/\alpha\text{-}MnO_2$ on the PMS activation for OG degradation, including PMS, $MnFe_2O_4$/PMS/OG,

326    $\alpha\text{-}MnO_2$/PMS/OG, $MnFe_2O_4/\alpha\text{-}MnO_2$/PMS/OG ($MnFe_2O_4/\alpha\text{-}MnO_2$ with different mass ratios of

327   1:5, 1:7, and 1:9), under the resembled experimental conditions. The conditions for conducting

328   experiments are as follows: [OG] = 50 mg/L, [PMS] = 1000 mg/L, [catalyst] = 100 mg/L, initial

329   pH = 3.0, temperature = 30 ^{o}C. As shown in **Figure 11a**, when only PMS was used, the reduction

330   efficiency in OG concentration was approximately 18%. Besides, the addition of the

331    $MnFe_2O_4$/PMS system was observed to induce only 38% in OG degradation. Meanwhile, almost

332   85% OG removal was adopted for the $\alpha\text{-}MnO_2$/PMS system. These results indicated that the PMS

333   activating capability of $\alpha\text{-}MnO_2$ was much greater than that of $MnFe_2O_4$. On the other hand, the

334   combined utilization of $MnFe_2O_4/\alpha\text{-}MnO_2$ catalyst and PMS can elicit a $MnFe_2O_4/\alpha\text{-}MnO_2$ mass

335   ratio-dependent OG degradation pattern. In particular, $MnFe_2O_4/\alpha\text{-}MnO_2$ (1:5)/PMS and

336    $MnFe_2O_4/\alpha\text{-}MnO_2$ (1:7)/PMS systems reduced OG concentration to the extents (sequentially 57%

337   and 82%) less than that of the above-mentioned $\alpha\text{-}MnO_2$/PMS system. The lower efficiencies in

338   OG degradation using $MnFe_2O_4/\alpha\text{-}MnO_2$ (1:5)/PMS and $MnFe_2O_4/\alpha\text{-}MnO_2$ (1:7)/PMS systems

339   implied that $\alpha\text{-}MnO_2$ possesses a predominant role in PMS activation while $MnFe_2O_4$ mostly

340   accounted for easy separation and reusability of the hybrid and that the $MnFe_2O_4$:$\alpha\text{-}MnO_2$ mass

341 ratios of 1:5 and 1:7 were insufficient to effectively activate PMS. In contrast, 96.8% of OG was

342 degraded after 30 min treatment with $MnFe_2O_4/\alpha$-MnO_2 (1:9)/PMS system. These results indicated

343 that the OG removal efficiency ascended with the arising of α-MnO_2 content in the composition

344 of $MnFe_2O_4/\alpha$-MnO_2 hybrid. Compared with α-MnO_2/PMS system, the enhancement in

345 $MnFe_2O_4/\alpha$-MnO_2 (1:9)/PMS-induced OG degradation could be ascribed to the increased surface

346 area and active sites for PMS activation that presumably due to the deposition of $MnFe_2O_4$

347 nanoparticles on the α-MnO_2 nanosheet surface. Moreover, the hybrid might possess a synergistic

348 effect between $MnFe_2O_4$ and α-MnO_2 in overall catalytic ability by reinforcing the relative rates of

349 mass transfer to PMS active sites and the relative rates of chemical reaction at these sites (Chen *et*

350 *al.*, 2019). Moreover, all results of OG degradation by PMS activation followed pseudo-first-order

351 reaction kinetics with $R^2 \geq 0.990$ (**Figure 11b**). The OG rate constant of $MnFe_2O_4/\alpha$-

352 MnO_2(1:9)/PMS was 1.66, 2, 4, 6.9, and 16 times higher than those of α-MnO_2/PMS, $MnFe_2O_4/\alpha$-

353 MnO_2(1:7)/PMS, $MnFe_2O_4/\alpha$-MnO_2(1:5)/PMS, $MnFe_2O_4$/PMS, and PMS, respectively. To

354 achieve a reasonable decomposition effect and reusability of catalysts, the $MnFe_2O_4/\alpha$-MnO_2

355 hybrid with a mass ratio of 1:9 was chosen as the optimal catalyst for further experiments. These

356 results are different with those reported in the literature for $MnFe_2O_4/MnO_2$(1:7)/PMS in

357 Rhodamine B removal (Chen *et al.*, 2019), $MnFe_2O_4/\delta$-MnO_2(1:4)/PMS for sulfadiazine removal

358 (Zhu *et al.*, 2021), and $MnFe_2O_4/\alpha$-MnO_2(1:5)/PMS for norfloxacin removal (Xu *et al.*, 2021). The

359 difference in $MnFe_2O_4/\alpha$-MnO_2 ratio (i.e., 1:9 for this study) with others in the literature could be

360 due to different material synthesis methods, targeted organic pollutants, and optimum solution pH

361 values.

362 Time-dependent UV-Vis absorption spectra of OG during the reaction were investigated in

363 the wavelength region of 280-600 nm (**Figure 12**). The result showed that prior to the activation

364   of PMS by $MnFe_2O_4/\alpha\text{-}MnO_2$, the OG contained a weak shoulder near 333 nm and a strong and

365   broad band in the visible region at $\lambda_{max} = 480$ nm. The 480 nm peak is attributed to the absorption

366   of $\pi\text{-}\pi^*$ bond of azo (–N = N–) moiety, while the 333 nm peak is assigned to the naphthalene ring

367   in the structure of OG (Zhou *et al.*, 2018a). Obviously, the results exhibited that the absorbance at

368   wavelengths of 333 and 480 nm steadily decreased over time. After 30 min, the characteristic

369   absorption peaks at 333 and 480 nm were significantly reduced and almost disappeared, indicating

370   that the azo bond and aromatic rings in the OG structure were entirely destroyed. These

371   observations could be ascribed to the attack of generated sulfate radicals to azo bond in the OG

372   after the exposure of $MnFe_2O_4/\alpha\text{-}MnO_2$ hybrid to PMS, which is also consistent with those

373   published by Wu *et al.* (2021).

374   **3.2.2. Effect of catalyst dosage**

375   The influence of catalyst dosage in the range of 50-125 mg/mL on the OG decomposition

376   was examined. The kinetics of OG degradation at different catalytic doses followed the pseudo-

377   first-order kinetics model with $R^2 \geq 0.991$ **(Figure 13b)**. As displayed in **Figure 13a** and **13b**,

378   when the dosage of $MnFe_2O_4/\alpha\text{-}MnO_2$ hybrid was changed from 50-100 mg/mL, the calculated

379   reaction rate constant *k* values were gradually elevated from 0.024-0.113 min^{-1} and thereby

380   increasing the OG degradation values from 50 to 96.8% after 30 min of treatment. The OG could

381   be entirely degraded when the catalyst dosage was 100 mg/mL. Importantly, there were no notable

382   differences in OG removal (only 2.2% enhancement) and *k* value (from 0.113 to 0.16) when the

383   catalyst dosage elevated from 100 to 125 mg/mL. These results implied that an increase of catalyst

384   dosage elicits more PMS active centers on the catalyst surface, thus leading to an improvement in

385   the capacity of activating PMS to create free radicals such as $SO_4^{\bullet-}$ and $HO^{\bullet}$. However, if the

386   catalyst dosage increases to a threshold, the number of active centers was not significantly mounted.

387   Therefore, the catalyst concentration of 100 mg/L was adopted for the next experiments.

3.2.3. Effect of temperature

389   Next, **Figure 14** demonstrates the effect of different reaction temperatures on removing OG,

390   showing that the OG removal was proportionally dependent on the reaction temperature. In

391   particular, the OG decomposition efficiency reached 41.2% at 20 ^oC in 30 min, whereas roughly

392   96.8% of initial OG was decomposed at 30 ^oC in the same period. By contrast, $MnFe_2O_4/\alpha$-

393   MnO_2 (1:9)/PMS treatment at 40 ^oC exhibited almost complete OG removal within a shorter period

394   (18 min). Moreover, the OG degradation process at different reaction temperatures followed a

395   pseudo-first-order kinetic model with the linear correlation coefficient $R^2 \geq 0.986$ (**Figures 14b**).

396   In particular, when the reaction temperature was elevated from 20 to 40^oC, the reaction rate

397   constant ascended remarkably from 0.04 min^{-1} to 0.232 min^{-1}. On the other hand, the relationship

398   between the reaction rate constant and reaction temperature was illustrated through the variant of

399   the Arrhenius equation:

$$k = C/C_0 = Ae^{-\frac{Ea}{RT}} \tag{Eq. 3}$$

401   Hence, $\ln k = \ln(C/C_0) = -\frac{Ea}{R}\frac{1}{T} + \ln A$ (Eq. 4)

402   Where k is the reaction rate constant and E_a is the activation energy of OG decomposition. T

403   is the absolute temperature (K) and R is the universal gas constant (8.314 J/(mol.K)). A is the

404   frequency or pre-exponential factor (constant).

405   As shown in **Figure 14b**, the decomposition rate constant at 40 ^oC was about 2.34- and 5.8-

406   folded greater than those at 30 and 20 ^oC, respectively. These experimental results were consistent

407   with the kinetics theory, which defines that when temperature increases 10 ^oC, the reaction rate

408   proportionally ascends 2-4 folds (Kralj and Chemistry, 2007). Furthermore, the activation energy

409   (E_a) of 66.90 kJ mol^{-1} was calculated (**Figures 14c**), which was different from the activation energy

410   values of the previous reports using other experimental systems (e.g., 42.7 KJ mol^{-1} for

411   MnFe$_2$O$_4$/δ-MnO$_2$/PMS system and 21.54 KJ mol^{-1} for α-MnO$_2$/MnFe$_2$O$_4$/PMS system (Xu *et al.*,

412   2021; Zhu *et al.*, 2021)). These observations implied that this heterogeneous catalyst system could

413   be monitored by the chemical reaction rate and it would be a potential agent for the PMS activation

414   for the treatment of organic pollutants in water.

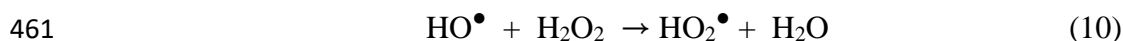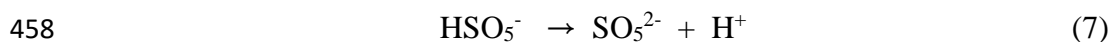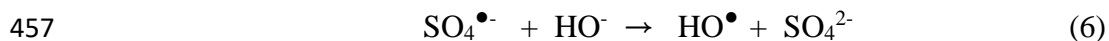415   **3.2.4. Effect of solution pH**

416   In the process of activating PMS by heterogeneous catalyst systems, the solution pH affects

417   the surface functional groups and surface charge of catalysts. Thus, a study on the effect of initial

418   pH on OG degradability was herein conducted in a pH range of 3.0-11.0, as described in **Figure**

419   **15**. Overall, the acidic and alkaline pH values had a strong influence on the OG decomposition

420   efficiency while this influence at neutral pH was rather low (**Figures 15a and 15b**). In addition,

421   the data at different pH fitted well with the pseudo-first-order kinetics with $R^2 \geq 0.97$, the *k* value

422   increased steadily in the acidic pH range (pH 3-5), then dropped rapidly at neutral pH (pH 7.0),

423   and eventually reached maxima in the alkaline pH range (pH 9-11) (**Figure 15b**). Evidently, the

424   OG amounts were removed of 96.8 and 97.19% after 30 min of treatment at pH 3 and 5,

425   respectively (**Figures 15a**). The strong degradation of OG in the acidic medium can be explained

426   as follows. The pHzpc of the hybrid material was determined to be 5.25 (**Figure 15c**). In an acidic

427   environment, the surface of MnFe$_2$O$_4$/α-MnO$_2$ is positively charged while HSO$_5^-$ (pK$_{a2}$ = 9.4) is a

428   predominant form of PMS species. Meanwhile, OG has a negative charge due to the existence of

429   anion HL^{2-} (with pH >1) since OG has pKa$_1$=1 (sulfonic groups (–SO$_3$H)) and pKa$_2$=11.5

430   (hydroxyl group (–OH)) (Hsini *et al.*, 2020; Zhou *et al.*, 2018b). Therefore, there is strong

431 adsorption of PMS and OG on the surface of the catalyst according to the electrostatic attraction

432 mechanism of the opposite ions, leading to an increase in PMS activating ability on the catalytic

433 surface to form active oxygen species for OG decomposition.

434 In neutral conditions (pH =7), the efficiency of OG decomposition declined to the lowest

435 value of 40.09% after 30 min of reaction. This result was assigned to the reduced electrostatic

436 interaction and adsorption of OG (in HL^{2-} form) and PMS (in HSO_5^- form) on the negatively

437 charged surface of the catalyst, leading to a decrease in the PMS activating ability and the

438 effectiveness of OG degradation. Thus, under acidic conditions, the $MnFe_2O_4/\alpha\text{-}MnO_2$/PMS

439 system favorably decomposes OG over neutral conditions (Wu $et\ al.$, 2021).

440 In addition, the OG decomposition occurs rapidly when the pH increases to reach an alkaline

441 environment. After 8 min, OG decomposition efficiencies were 97.1 and 97.6% at pH 9 and 11,

442 respectively. In the alkaline environment, PMS and OG correspondingly exist in forms of SO_5^{2-}

443 and HL^{2-}, thus resulting in the reduced electrostatic interaction and absorption of PMS and OG on

444 the negatively charged surface of the catalyst. Theoretically, the OG decomposition efficiency

445 would be drastically reduced. However, in terms of the experiment results, it is observed that the

446 OG decomposition takes place quickly under alkaline conditions, which can be explained as

447 follows. The existence of SO_5^{2-} form leads to the formation of active oxygen species (e.g., $HO^\bullet$,

448 $O_2^{\bullet-}$, and $^1O_2$) which hold redox potentials of 2.8, 2.4, and 2.2 V, respectively (Reaction 6-11).

449 These active oxygen types have strong oxidizing properties, thereby rapidly decomposing OG into

450 mineralized products, which was also mentioned in several previous studies (Wu $et\ al.$, 2021; Xu

451 $et\ al.$, 2021). However, some studies showed that the $\alpha\text{-}MnO_2$-based hybrid material was

452 negatively affected by the alkaline environment in organics removal (Chen $et\ al.$, 2019; Huang et

453 $al.$, 2020). Thus, the $MnFe_2O_4/\alpha\text{-}MnO_2$/PMS system exhibits high degradability of OG in a wide

454   range of pH from 3.0 to 11.0, which unveils the potential of using $MnFe_2O_4/\alpha\text{-}MnO_2$ as a catalyst

455   to decompose organic pollutants in various industrial wastewaters from tanning, printing, dyeing,

456   pulp/paper, and petrochemical manufacturing.

457   $$SO_4^{\bullet-} + HO^- \rightarrow HO^\bullet + SO_4^{2-} \qquad\qquad (6)$$

458   $$HSO_5^- \rightarrow SO_5^{2-} + H^+ \qquad\qquad (7)$$

459   $$HSO_5^- + SO_5^{2-} \rightarrow HSO_4^- + {}^1O_2 \qquad\qquad (8)$$

460   $$SO_5^{2-} + H_2O \rightarrow H_2O_2 + SO_4^{2-} \qquad\qquad (9)$$

461   $$HO^\bullet + H_2O_2 \rightarrow HO_2^\bullet + H_2O \qquad\qquad (10)$$

462   $$HO_2^\bullet \rightarrow H^+ + O_2^{\bullet-} \qquad\qquad (11)$$

463   For the $MnFe_2O_4/\alpha\text{-}MnO_2$/PMS system with solution pH = 3.0, it does not have to adjust the pH

464   of the solution, and the efficiency of OG degradation was high at this pH (96.8%) after 30 min

465   treatment (Huang *et al.*, 2019; Lyu *et al.*, 2019). Therefore, pH 3.0 was chosen for further studies.

466   **3.2.5. Reusability of magnetic $MnFe_2O_4/\alpha\text{-}MnO_2$ hybrid**

467   To evaluate the stability and reusability of $MnFe_2O_4/\alpha\text{-}MnO_2$ catalyst, after each OG

468   experimental treatment, the catalyst was adopted by using magnetic separation, washed once with

469   DI water and three times with ethanol, dried at 80 $^\circ$C for 12 hours in a vacuum oven before being

470   continuously reused for a new cycle (of total 4 cycles) under the optimal conditions (i.e., [OG] =

471   50 mg/L, [PMS] = 1000 mg/L, [catalyst] = 100 mg/L, initial pH = 3.0, temperature = 30 $^\circ$C). As

472   shown in **Figure 16**, after four continuous cycles, the $MnFe_2O_4/\alpha\text{-}MnO_2$ (1:9)/PMS system

473   presented an approximately 30% decrease in OG removal. This slight reduction in OG degradation

474   could be attributed to either a partial loss of catalyst during recovery processes or residual

475   contaminants on active sites of the catalyst surface. Overall, the result demonstrated that the

476   catalyst possesses relatively high recyclability and reusability, which contribute to the reduction

477   in expenses for wastewater treatment and used catalyst amount.

478   **3.3. Comparison with other works**

479   Herein, the PMS activation capacity of different heterogeneous catalysts on the basis of the

480   elements Mn and Fe for decomposition of organic pollutants was compared (Zhu *et al.*, 2021; Chen

481   *et al.*, 2019; Huang *et al.*, 2020; Lyu *et al.*, 2019; Fu *et al.*, 2019; Deng *et al.*, 2016). As shown in

482   **Table 2**, OG (50 mg/L) is completely decomposed by the $MnFe_2O_4$/α-MnO_2/PMS system in a

483   short time of 30 min with a high OG degradation rate constant of 0.113 min^{-1} with a low catalyst

484   dosage of 100 mg/L. Different active oxygen types such as $SO_4^{\bullet-}$, $O_2^{\bullet-}$, and $^1O_2$ all contribute to

485   the decomposition of OG. This comparison shows that the performance of the $MnFe_2O_4$/α-MnO_2

486   /PMS system is excellent and promising for practical applications in wastewater treatment.

487   **3.4. Mechanism of $MnFe_2O_4$/α-MnO_2/PMS system for OG degradation**

488   **3.4.1. Identification of reactive oxygen species in the $MnFe_2O_4$/α-MnO_2 /PMS system**

489   The PMS activation process by the $MnFe_2O_4$/α-MnO_2 system can directly form active

490   oxygen types such as $SO_4^{\bullet-}$ and $HO^{\bullet}$. Other active oxygen species such as $O_2^{\bullet-}$ and $^1O_2$ are

491   generated through intermediate reactions. To identify the active oxygen types formed in the

492    $MnFe_2O_4$/α-MnO_2/PMS system, various organic solvents were used as the quenching agents of

493   active oxygen types such as tert-butanol (TBA), ethanol (EtOH), FFA with a concentration of

494   100mM, and p-BQ with a concentration of 10mM. The basis of solvent selection is as follows.

495   The reaction rate constant of tert-butanol (TBA) with $HO^{\bullet}$ is faster than $SO_4^{\bullet-}$ from 835 to 950

496   times ($k_{TBA-HO^{\bullet}} = 3.8\text{-}7.6\times10^8$ $M^{-1}.s^{-1}$; $k_{TBA-SO4^{\bullet-}} = 4.0\text{-}9.1\times10^5$ $M^{-1}.s^{-1}$); therefore, tert-butanol

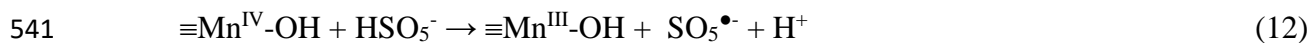497   (TBA) was chosen as the decomposing agent of hydroxyl radical ($HO^{\bullet}$). Both reaction rate

498   constants of EtOH with $HO^{\bullet}$ ($k_{EtOH-HO\bullet} = 1.2$-2.8×10^9 $M^{-1}.s^{-1}$) and with $SO_4^{\bullet-}$ ($k_{EtOH-SO4\bullet-} = 1.6$-

499   7.7×10^7 $M^{-1}.s^{-1}$) are high. Thus, ethanol was selected as the degrading agent of both $HO^{\bullet}$ and $SO_4^{\bullet-}$

500   free radicals. p-BQ was selected for the decomposition of $O_2^{\bullet-}$ radicals due to its high reaction rate

501   constant with $O_2^{\bullet-}$ ($k_{p-BQ-O2\bullet-} = 0.9$-$1.0\times10^9$ $M^{-1}.s^{-1}$), leading to its capability in radical $O_2^{\bullet-}$

502   quenching. FFA was chosen as decomposing agent of $^1O_2$ and $HO^{\bullet}$ radicals due to its high reaction

503   rate with both $^1O_2$ and $HO^{\bullet}$ ($k_{FFA-1O2} = 1.2\times10^8$ $M^{-1}.s^{-1}$; $k_{FFA-HO\bullet} = 1.5\times10^{10}$ $M^{-1}.s^{-1}$) (Huang *et al.*,
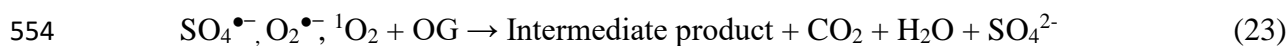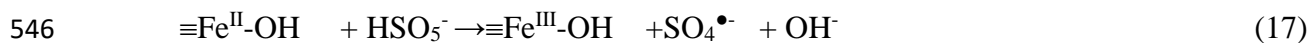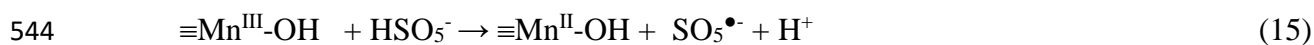
504   2019).

505   **Figure 17** shows that for a blank sample (no scavengers), 96.8% OG was decomposed by

506   the $MnFe_2O_4/\alpha$-MnO_2/PMS system after 30 min. When adding TBA, FFA, p-BQ, and EtOH with

507   a concentration of 100 mM (for TBA, FFA, and EtOH) and 10 mM (for p-BQ), the decomposition

508   efficiency decreased to 83.8, 36.68, 24.6, and 11.32%, respectively. These results unveiled that the

509   decomposition capability of active oxygen species generated from the $MnFe_2O_4/\alpha$-MnO_2/PMS

510   system is in the order of $SO_4^{\bullet-} > O_2^{\bullet-} > {}^1O_2 > HO^{\bullet}$. Hence, EtOH, p-BQ, and FFA greatly inhibited

511   the OG degradation, indicating that $SO_4^{\bullet-}$, $O_2^{\bullet-}$, and $^1O_2$ in $MnFe_2O_4/\alpha$-MnO_2/PMS have a decisive

512   role in OG removal. This is different from the literature about the $MnFe_2O_4/MnO_2$/PMS and

513    $MnFe_2O_4/\delta$-MnO_2/PMS system, where $SO_4^{\bullet-}$ was identified as the key radical for degradation of

514   Rhodamine B (Chen *et al.*, 2019) and Sulfadiazine (Zhu *et al.*, 2021), and α-

515   MnO_2/Palygorskite/PMS and β-FeOOH/MnO_2/PMS systems, where $O_2^{\bullet-}$ and $^1O_2$ are the key

516   radicals for Rhodamine B (Huang *et al.*, 2020) and Orange II (Lyu *et al.*, 2019) degradation. These

517   different conclusions in the role of the key radicals for organics pollutants could be due to the

518   different solution pH, which leads to the formation of different radicals during the PMS activation.

519   **3.2.2. Mechanism of PMS activation by $MnFe_2O_4/\alpha$-MnO_2 catalyst**

520   Based on the experimental results, the mechanism of PMS activation by $MnFe_2O_4$ /α-MnO_2

521   catalyst is proposed as follows. First, HSO_5^- in solution is adsorbed on the surface of $MnFe_2O_4$/α-

522   MnO_2. Then, manganese oxides (α-MnO_2) containing Mn active centers with different valences

523   (i.e., Mn^{IV}, Mn^{III}, and Mn^{II}) interact with HSO_5^- to form $SO_5^{\bullet-}$ and $SO_4^{\bullet-}$ radicals (Reactions 12-

524   15). In addition, Fe^{III} and Fe^{II} on the catalytic surface also participate in the formation of $SO_5^{\bullet-}$ and

525    $SO_4^{\bullet-}$ radicals (Reactions 16-17). On the other hand, the reaction between Fe^{2+} and Mn^{4+} to form

526   Fe^{3+} and Mn^{3+} is thermodynamically favorable since the standard potentials of Mn^{IV}/Mn^{III} and

527   Fe^{III}/Fe^{II} are 0.95 and 0.77 V, respectively (Reaction 18) (Chen *et al.*, 2019). The sulfate radical

528   ($SO_4^{\bullet-}$) is partially converted to hydroxyl radical ($HO^\bullet$) in the presence of water (Reaction 19).

529   HSO_5^- is destabilized in H_2O, thereby converting to H_2O_2 (Reaction 20). Hydroxyl radical ($HO^\bullet$)

530   is decomposed by H_2O_2 to form hydroperoxyl radical ($HO_2^\bullet$) (Reaction 10), and then the

531   hydroperoxyl radical decomposes into superoxide radical ($O_2^{\bullet-}$) (Reaction 11). Superoxide

532   radicals can react with both proton (H^+) and hydroxyl radical ($HO^\bullet$) to form singlet oxygen ($^1O_2$)

533   (Reaction 21-22).

534   Among the active oxygen types, $SO_5^{\bullet-}$ and $HO_2^\bullet$ have weak oxidizing properties (1.1 V

535   and 1.65V, respectively), while other species including $SO_4^{\bullet-}$ (2.8-3.1 V), $O_2^{\bullet-}$ (2.4 V), and $^1O_2$

536   (2.2 V) possess stronger oxidizing activities, which mainly account for the decomposition of OG

537   in water. Thus, the mechanism of PMS activation by $MnFe_2O_4$/α-MnO_2 catalyst is proposed in

538   **Figure 18**. This mechanism is determined by the Mn^{IV}/Mn^{III} and Fe^{III}/Fe^{II} redox pairs. Moreover,

539    $SO_4^{\bullet-}$, $O_2^{\bullet-}$, and $^1O_2$ radicals were determined to be the dominant reactive oxygen species in the

540    $MnFe_2O_4$/α-MnO_2/PMS system that are responsible for the decomposition of OG.

541    $$\equiv Mn^{IV}\text{-}OH + HSO_5^- \rightarrow \equiv Mn^{III}\text{-}OH + SO_5^{\bullet-} + H^+ \tag{12}$$

542    $$\equiv Mn^{III}\text{-}OH + HSO_5^- \rightarrow \equiv Mn^{IV}\text{-}OH + SO_4^{\bullet-} + OH^- \tag{13}$$

543      $\equiv Mn^{II}\text{-}OH + HSO_5^- \rightarrow \equiv Mn^{III}\text{-}OH + SO_4^{\bullet-} + OH^-$ (14)

544      $\equiv Mn^{III}\text{-}OH + HSO_5^- \rightarrow \equiv Mn^{II}\text{-}OH + SO_5^{\bullet-} + H^+$ (15)

545      $\equiv Fe^{III}\text{-}OH + HSO_5^- \rightarrow \equiv Fe^{II}\text{-}OH + SO_5^{\bullet-} + H^+$ (16)

546      $\equiv Fe^{II}\text{-}OH + HSO_5^- \rightarrow \equiv Fe^{III}\text{-}OH + SO_4^{\bullet-} + OH^-$ (17)

547      $\equiv Fe^{II}\text{-}OH + \equiv Mn^{IV}\text{-}OH \rightarrow \equiv Fe^{III}\text{-}OH + \equiv Mn^{III}\text{-}OH$ (18)

548      $SO_4^{\bullet-} + H_2O \rightarrow HO^{\bullet} + SO_4^{2-} + H^+$ (19)

549      $HSO_5^- + H_2O \rightarrow H_2O_2 + HSO_4^-$ (20)

550      $HO^{\bullet} + H_2O_2 \rightarrow HO_2^{\bullet} + H_2O$ (10)

551      $HO_2^{\bullet} \rightarrow O_2^{\bullet-} + H^+$ (11)

552      $2O_2^{\bullet-} + H^+ \rightarrow {}^1O_2 + H_2O_2 + 2HO^-$ (21)

553      $2O_2^{\bullet-} + HO^{\bullet} \rightarrow {}^1O_2 + H_2O_2$ (22)

554      $SO_4^{\bullet-}, O_2^{\bullet-}, {}^1O_2 + OG \rightarrow \text{Intermediate product} + CO_2 + H_2O + SO_4^{2-}$ (23)

555

4. Conclusions

557   In this study, a well-crystallized magnetic $MnFe_2O_4/\alpha\text{-}MnO_2$ hybrid with high purity was

558 successfully synthesized via a new hydrothermal method and characterized by XRD, SEM, EDX,

559 XPS, FT-IR, SEM, and BET. The synthesized hybrid material showed catalytic activity in PMS

560 activation for OG degradation to the extent greater than that of bare $MnFe_2O_4$ and $\alpha\text{-}MnO_2$. The

561 parameters including initial pH, temperature, and catalyst dosage were revealed to be crucial for

562 the OG removal. The results from quenching experiments indicated that $SO_4^{\bullet-}$, $O_2^{\bullet-}$, and ${}^1O_2$

563 radicals were responsible for OG degradation. It was unveiled that the OG removal efficiency had

564 less than 30% loss after four consecutive cycles, which implied the good stability of the

565 $MnFe_2O_4/\alpha\text{-}MnO_2$ material. Overall, the heterogeneous $MnFe_2O_4/\alpha\text{-}MnO_2$ hybrid emerges as a

566 promising PMS activator for the treatment of wastewater containing OG and maybe other dyes.

567

References

569 Cai M, Jin M, Weavers L K, 2011. Analysis of sonolytic degradation products of azo dye Orange

570   G using liquid chromatography–diode array detection-mass spectrometry. *Ultrasonics*

571   *Sonochemistry*, 18(5)1068-1076.

572 Cai W, Lai T, Dai W, Ye J, 2014. A facile approach to fabricate flexible all-solid-state

573   supercapacitors based on MnFe2O4/graphene hybrids. *Journal of Power Sources*, 255170-178.

574 Chen G, Zhang X, Gao Y, Zhu G, Cheng Q, Cheng X, 2019. Novel magnetic MnO2/MnFe2O4

575   nanocomposite as a heterogeneous catalyst for activation of peroxymonosulfate (PMS) toward

576   oxidation of organic pollutants. *Separation and Purification Technology*, 213456-464.

577 Davoglio R A, Cabello G, Marco J F, Biaggio S R, 2018. Synthesis and characterization of α-

578   MnO2 nanoneedles for electrochemical supercapacitors. *Electrochimica Acta*, 261428-435.

579 Deng J, Feng S, Ma X, Tan C, Wang H, Zhou S, Zhang T, Li J J S, Technology P, 2016.

580   Heterogeneous degradation of Orange II with peroxymonosulfate activated by ordered

581   mesoporous MnFe2O4. 167181-189.

582 Dong Y, Li K, Jiang P, Wang G, Miao H, Zhang J, Zhang C, 2014. Simple hydrothermal

583   preparation of α-, β-, and γ-MnO2 and phase sensitivity in catalytic ozonation. *RSC Advances*,

584   4(74)39167-39173.

585 Ejder-Korucu M, Gürses A, Doğar Ç, Sharma S K, Açıkyıldız M, 2015. Removal of Organic Dyes

586   from Industrial Effluents: An Overview of Physical and Biotechnological Applications. *Green*

587   *Chemistry for Dyes Removal from Wastewater*, 1-34.

588 Fan Y, Ma W, He J, Du Y, 2017. CoMoO4 as a novel heterogeneous catalyst of peroxymonosulfate

589   activation for the degradation of organic dyes. *RSC Advances*, 7(57)36193-36200.

590 Fu H, Ma S, Zhao P, Xu S, Zhan S J C E J, 2019. Activation of peroxymonosulfate by graphitized

591   hierarchical porous biochar and MnFe2O4 magnetic nanoarchitecture for organic pollutants

592   degradation: Structure dependence and mechanism. 360157-170.

593 Garrido-Cardenas J A, Esteban-García B, Agüera A, Sánchez-Pérez J A, Manzano-Agugliaro F,

594   2019. Wastewater Treatment by Advanced Oxidation Process and Their Worldwide Research

595   Trends. *Int J Environ Res Public Health*, 17(1)

596 Hsini A, Essekri A, Aarab N, Laabd M, Addi A A, Lakhmiri R, Albourine A J E S, Research P,

597   2020. Elaboration of novel polyaniline@ Almond shell biocomposite for effective removal of

598   hexavalent chromium ions and Orange G dye from aqueous solutions. 1-14.

599 Hu P, Long M, 2016. Cobalt-catalyzed sulfate radical-based advanced oxidation: A review on

600   heterogeneous catalysts and applications. *Applied Catalysis B: Environmental*, 181103-117.

601 Huang C, Wang Y, Gong M, Wang W, Mu Y, Hu Z-H, 2020. α-MnO$_2$/Palygorskite composite as

602   an effective catalyst for heterogeneous activation of peroxymonosulfate (PMS) for the

603   degradation of Rhodamine B. *Separation and Purification Technology*, 230115877.

604 Huang J, Dai Y, Singewald K, Liu C-C, Saxena S, Zhang H J C E J, 2019. Effects of MnO2 of

605   different structures on activation of peroxymonosulfate for bisphenol A degradation under

606   acidic conditions. 370906-915.

607 Huang J, Zhang H, 2019. Mn-based catalysts for sulfate radical-based advanced oxidation

608   processes: A review. *Environment International*, 133105141.

609 Javaid R, Qazi U Y, 2019. Catalytic Oxidation Process for the Degradation of Synthetic Dyes: An

610   Overview. *International journal of environmental research and public health*, 16(11)2066.

611 Kralj A K J J o I, Chemistry E, 2007. Checking the kinetics of acetic acid production by measuring

612   the conductivity. 13(4)631-636.

613 Kurtan U, Amir M, Yıldız A, Baykal A, 2016. Synthesis of magnetically recyclable

614 MnFe2O4@SiO2@Ag nanocatalyst: Its high catalytic performances for azo dyes and nitro

615 compounds reduction. *Applied Surface Science*, 37616-25.

616 Li Y, Dong H, Li L, Tang L, Tian R, Li R, Chen J, Xie Q, Jin Z, Xiao J, Xiao S, Zeng G, 2021.

617 Recent advances in waste water treatment through transition metal sulfides-based advanced

618 oxidation processes. *Water Research*, 192116850.

619 Lyu C, He D, Mou Z, Yang X J S o T T E, 2019. Synergetic activation of peroxymonosulfate by

620 MnO2-loaded β-FeOOH catalyst for enhanced degradation of organic pollutant in water.

621 693133589.

622 M'Arimi M M, Mecha C A, Kiprop A K, Ramkat R, 2020. Recent trends in applications of

623 advanced oxidation processes (AOPs) in bioenergy production: Review. *Renewable and*

624 *Sustainable Energy Reviews*, 121109669.

625 Ma H, Shen J, Shi M, Yan B, Li N, Ye M, 2011. Facile and template-free preparation of α-MnO2

626 nanostructures and their enhanced adsorbability. *Materials Research Bulletin*, 46(9)1461-1466.

627 Ma J, Ding Y, Chi L, Yang X, Zhong Y, Wang Z, Shi Q, 2021. Degradation of benzotriazole by

628 sulfate radical-based advanced oxidation process. *Environmental Technology*, 42(2)238-247.

629 Peng Y, Tang H, Yao B, Gao X, Yang X, Zhou Y, 2021. Activation of peroxymonosulfate (PMS)

630 by spinel ferrite and their composites in degradation of organic pollutants: A Review. *Chemical*

631 *Engineering Journal*, 414128800.

632 Pham V T, T. Nguyen H-T, Thi Cam Nguyen D, T. N. Le H, Thi Nguyen T, Thi Hong Le N, Lim

633 K T, Duy Nguyen T, Tran T V, Bach L G, 2019. Process Optimization by a Response Surface

634 Methodology for Adsorption of Congo Red Dye onto Exfoliated Graphite-Decorated

635 MnFe2O4 Nanocomposite: The Pivotal Role of Surface Chemistry. *Processes*, 7(5)

636   Reddy M P, Mohamed A M A, 2015. One-pot solvothermal synthesis and performance of

637   mesoporous magnetic ferrite MFe$_2$O$_4$ nanospheres. *Microporous and Mesoporous Materials*,

638   21537-45.

639   Shao L, Ren Z, Zhang G, Chen L, 2012. Facile synthesis, characterization of a MnFe2O4/activated

640   carbon magnetic composite and its effectiveness in tetracycline removal. *Materials Chemistry*

641   *and Physics*, 135(1)16-24.

642   Sotomayor F J, Cychosz K A, Thommes M J A M S R, 2018. Characterization of

643   micro/mesoporous materials by physisorption: concepts and case studies. 3(2)34-50.

644   Uematsu T, Miyamoto Y, Ogasawara Y, Suzuki K, Yamaguchi K, Mizuno N, 2016. Molybdenum-

645   doped α-MnO2 as an efficient reusable heterogeneous catalyst for aerobic sulfide oxygenation.

646   *Catalysis Science & Technology*, 6(1)222-233.

647   Wang H, Lu Z, Qian D, Li Y, Zhang W, 2007. Single-crystal α-MnO2nanorods: synthesis and

648   electrochemical properties. *Nanotechnology*, 18(11)115616.

649   Wang J, Zhuan R, 2020. Degradation of antibiotics by advanced oxidation processes: An overview.

650   *Science of The Total Environment*, 701135023.

651   Wu M, Wang Y, Lu B, Xiao B, Chen R, Liu H, 2021. Efficient activation of peroxymonosulfate

652   and degradation of Orange G in iron phosphide prepared by pickling waste liquor.

653   *Chemosphere*, 269129398.

654   Xia X, Zhu F, Li J, Yang H, Wei L, Li Q, Jiang J, Zhang G, Zhao Q, 2020. A Review Study on

655   Sulfate-Radical-Based Advanced Oxidation Processes for Domestic/Industrial Wastewater

656   Treatment: Degradation, Efficiency, and Mechanism. *Frontiers in Chemistry*, 81092.

657   Xie Y, Yu Y, Gong X, Guo Y, Guo Y, Wang Y, Lu G, 2015. Effect of the crystal plane figure on

658   the catalytic performance of MnO2 for the total oxidation of propane. *CrystEngComm*,

659   17(15)3005-3014.

660   Xu L S, Sun X B, Hong J-m, Zhang Q, 2021. Peroxymonosulfate activation by α-MnO2/MnFe2O4

661   for norfloxacin degradation: Efficiency and mechanism. *Journal of Physics and Chemistry of*

662   *Solids*, 153110029.

663   Yao Y, Cai Y, Lu F, Wei F, Wang X, Wang S, 2014. Magnetic recoverable MnFe2O4 and

664   MnFe2O4-graphene hybrid as heterogeneous catalysts of peroxymonosulfate activation for

665   efficient degradation of aqueous organic pollutants. *Journal of Hazardous Materials*, 27061-

666   70.

667   Zhang X, Li B, Li X, Chu Q, Yang M, Wang X, Chen H, Peng L, Liu X, 2014. Morphology-

668   controlled synthesis and growth mechanisms of branched α-MnO2 nanorods via facile

669   microwave-assisted hydrothermal method. *Journal of Materials Science: Materials in*

670   *Electronics*, 25(2)906-913.

671   Zhou F, Yan C, Liang T, Sun Q, Wang H, 2018a. Photocatalytic degradation of Orange G using

672   sepiolite-TiO2 nanocomposites: Optimization of physicochemical parameters and kinetics

673   studies. *Chemical Engineering Science*, 183231-239.

674   Zhou F, Yan C, Liang T, Sun Q, Wang H J C E S, 2018b. Photocatalytic degradation of Orange G

675   using sepiolite-TiO2 nanocomposites: Optimization of physicochemical parameters and

676   kinetics studies. 183231-239.

677   Zhu L, Shi Z, Deng L, Duan Y, 2021. Efficient degradation of sulfadiazine using magnetically

678   recoverable MnFe2O4/δ-MnO2 hybrid as a heterogeneous catalyst of peroxymonosulfate.

679   *Colloids and Surfaces A: Physicochemical and Engineering Aspects*, 609125637.

680

681

Figure captions

683 **Figure 1.** The molecular structure of Orange G

684 **Figure 2.** Schematic illustration for the formation of $MnFe_2O_4/\alpha$-MnO_2

685 **Figure 3.** SEM images of (a-b) α-MnO_2, (c-d) $MnFe_2O_4$, and (e-f) $MnFe_2O_4/\alpha$-MnO_2

686 **Figure 4.** (a) EDX spectrum and (b) EDX mapping (O, Mn, Fe elements) of the $MnFe_2O_4/\alpha$-

687 MnO_2 hybrid

688 **Figure 5.** XRD patterns of α-MnO_2, $MnFe_2O_4$, and $MnFe_2O_4/\alpha$-MnO_2

689 **Figure 6.** FT-IR spectra of α-MnO_2, $MnFe_2O_4$, and $MnFe_2O_4/\alpha$-MnO_2

690 **Figure 7**. (a) Wide survey XPS spectrum, (b) Fe 2p spectrum, (c) Mn 2p spectrum, and (d) O 1s

691 spectrum of the $MnFe_2O_4/\alpha$-MnO_2 hybrid (Binding energy (BE) values were corrected using the

692 carbon peak at 284.6 eV as a reference)

693 **Figure 8.** TGA measurements of (a) α-MnO_2, (b) $MnFe_2O_4$, and (c) $MnFe_2O_4/\alpha$-MnO_2

694 **Figure 9.** (a) N_2 adsorption-desorption isotherms of $MnFe_2O_4/\alpha$-MnO_2 and (b) pore size

695 distribution of $MnFe_2O_4/\alpha$-MnO_2

696 **Figure 10.** The magnetization curve of magnetic $MnFe_2O_4/\alpha$-MnO_2

697 **Figure 11.** (a) Effects of different experimental systems on the decomposition of OG, (b) pseudo-

698 first-order kinetic linear regressions. (Experimental conditions: [OG] = 50 mg/L, [PMS] = 1000

699 mg/L, [catalyst] = 100 mg/L, initial pH = 3.0, and temperature = 30 ^{o}C)

700 **Figure 12.** Time-dependent UV-Vis spectral absorption of OG solution

701 **Figure 13.** Effect of different catalyst dosages on the decomposition of OG, (b) pseudo-first-order

702 kinetic linear regressions of different catalyst dosages on OG decomposition. (Experimental

703 conditions: [OG] = 50 mg/L, [PMS] = 1000 mg/L, initial pH = 3.0, and temperature = 30 ^{o}C)

704   **Figure 14.** Effect of different temperature conditions on the decomposition of OG, (b) pseudo-

705   first-order kinetic linear regressions of different temperature conditions on OG decomposition, (c)

706   Arrhenius plot of OG decomposition at different temperature conditions, which determines the

707   activation energy (E_a) of the system. (Experimental conditions: [OG] = 50 mg/L, [PMS] = 1000

708   mg/L, [catalyst] = 100 mg/L, initial pH = 3.0)

709   **Figure 15.** Effect of different pH conditions on the decomposition of OG, (b) pseudo-first-order

710   kinetic linear regressions of different pH conditions on OG decomposition, (c) pHpzc plot of

711     $MnFe_2O_4/\alpha\text{-}MnO_2$. (Experimental conditions: [OG] = 50 mg/L, [PMS] = 1000 mg/L, [catalyst] =

712   100 mg/L, initial pH = 3.0, and temperature = 30 ^oC)

713   **Figure 16.** The reuse efficiency of $MnFe_2O_4/\alpha\text{-}MnO_2$ catalyst on the decomposition of OG

714   (Experimental conditions: [OG] = 50 mg/L, [PMS] = 1000 mg/L, [catalyst] = 100 mg/L, initial pH

715   = 3.0, and temperature = 30 ^oC)

716   **Figure 17.** Influence of different radical scavengers on OG degradation in $MnFe_2O_4/\alpha\text{-}MnO_2/PMS$

717   system (Experimental conditions: [OG] = 50 mg/L, [PMS] = 1000 mg/L, [catalyst] = 100 mg/L,

718   [scavenger] = 100 mM, [p-BQ] = 10 mM, pH = 3.0, and temperature = 30 ^oC)

719   **Figure 18.** Mechanism of PMS activation by the $MnFe_2O_4/\alpha\text{-}MnO_2$ catalyst for radical generation

720   and OG degradation

721

722 **Table captions**

723 **Table 1**. Specific surface area, pore size, and pore volume of α-MnO$_2$, MnFe$_2$O$_4$, and MnFe$_2$O$_4$/α-

724 MnO$_2$

725 **Table 2.** Comparison of the decomposition of organic pollutants by PMS activation with

726 heterogeneous catalysts on the basis of Mn and Fe

727